

Fabrication and characterization of a co-planar detector in diamond for low energy single ion implantation

J. B. S. Abraham, B. A. Aguirre, J. L. Pacheco, G. Vizkelethy, and E. Bielejec

Citation: *Appl. Phys. Lett.* **109**, 063502 (2016); doi: 10.1063/1.4960968

View online: <http://dx.doi.org/10.1063/1.4960968>

View Table of Contents: <http://aip.scitation.org/toc/apl/109/6>

Published by the [American Institute of Physics](#)

Fabrication and characterization of a co-planar detector in diamond for low energy single ion implantation

J. B. S. Abraham,^{a)} B. A. Aguirre, J. L. Pacheco, G. Vizkelethy, and E. Bielejec
 Sandia National Laboratories, Albuquerque, New Mexico 87185, USA

(Received 16 May 2016; accepted 2 August 2016; published online 9 August 2016)

We demonstrate low energy single ion detection using a co-planar detector fabricated on a diamond substrate and characterized by ion beam induced charge collection. Histograms are taken with low fluence ion pulses illustrating quantized ion detection down to a single ion with a signal-to-noise ratio of approximately 10. We anticipate that this detection technique can serve as a basis to optimize the yield of single color centers in diamond. The ability to count ions into a diamond substrate is expected to reduce the uncertainty in the yield of color center formation by removing Poisson statistics from the implantation process. *Published by AIP Publishing.*

[<http://dx.doi.org/10.1063/1.4960968>]

Color centers in diamond have attracted significant attention due to successful demonstrations in the fields of quantum information,¹ metrology,² and biological systems.³ Although many types of color centers are known to exist in diamond,⁴ the majority of the demonstrations involve the Nitrogen-Vacancy (NV) and the Silicon-Vacancy (SiV) centers.¹ Recently, certain advantages of the SiV center over the NV have come to light. The SiV center is a more efficient source of indistinguishable photons with narrower linewidths and higher spectral stability.⁵ Furthermore, recent experiments indicate that the SiV center has stable optical properties after implantation into nanostructures,⁶ a critical requisite for viably integrating a color center with a device. There are two requirements to realizing color center based devices: spatial control and a well-defined color center formation yield.⁷

Spatial control has been achieved by ion implantation through either a suitable masking of a broad beam⁸ or the use of a focused ion beam.⁹ These techniques have resulted in nanometer scale control over the implant location. In these studies, it was found that the yield of color centers is relatively low 7% in Ref. 8, 15% in Ref. 9 and subject to Poisson statistics. In this context, yield is defined as the number of centers activated in proportion to the number of atoms introduced into the substrate via implantation. To date, work^{10,11} done to improve the yield of NV centers has advanced the understanding of center production and indicated a path for yield improvement by increasing the number of vacancies but has not completely resolved the challenge. Additionally, while a low yield may be acceptable for many applications, an uncertain yield is an impediment to the fabrication of color center based devices.

We propose controlled implantation as an approach to the question of yield improvement, namely, reducing the uncertainty in the yield by removing a source of Poisson statistics from the implantation process. We do so by adapting techniques developed for controlled implantation into Silicon,^{12–14} where *in-situ* single ion detectors in a silicon substrate allow for the counting of implanted ions. This will

allow for the removal of the uncertainty of the number of implanted ions in the diamond substrates resulting in a more precise understanding of additional factors which go into yield such as the role of the local population of vacancies, annealing parameters, and surface termination.^{10,11,15,16}

In this article, we report on a detector fabricated on a diamond substrate used to detect 200 keV Silicon ions. We show that the detector is capable of resolving single ion implants with high fidelity: the single ion signal has essentially no overlap with the noise floor. This implant is chosen because this energy is relevant for creating SiV centers at a shallow depth (on the order of 100 nm below the surface as modelled using a stopping and range of ions in matter (SRIM)¹⁷ simulation) to couple with nano-phonic structures. Secondary ion mass spectroscopy (SIMS) measurements of depth profiles of Silicon implanted into diamond confirm the expected depth.¹⁸

As a preface to describing the detector, we begin with a brief summary of ion detection via ionization. When an ion is implanted in a material, electron-hole (e-/h) pairs are generated by the interaction of the ion with the host atoms. The e-/h pairs can be detected by applying an electric field to the substrate. As the excess carriers move in the presence of the electric field, they induce a current on the electrodes supplying the field. This is described by the Gunn theorem¹⁹

$$i = q\vec{v} \cdot \frac{\partial \vec{E}}{\partial V}, \quad (1)$$

where \vec{E} is the electric field, V is applied bias on the detecting electrode, \vec{v} is the velocity of the charge carrier, and q is the charge. As a corollary to this theorem, the maximum induced charge is equal to the total generated ionization per ion.²⁰ Traps and defects of the substrate typically reduce the amount of ionization detected.²⁵ The charge collection efficiency (CCE) is the ratio of the collected charge to the deposited charge. Currently, chemical vapor deposition (CVD) diamond can be fabricated with a CCE approaching 95% in the bulk.^{21,22}

Diamond based radiation detectors have typically been used in high energy alpha and gamma (>1 MeV) applications.²³ At these energies, the range of the ionization is $\gg 1 \mu\text{m}$; as a result, the detection electrodes are on opposing

^{a)} Author to whom correspondence should be addressed. Electronic mail: jabrah@sandia.gov

sides of diamond substrates and the sensitive region is the entire thickness of the substrate.²⁴ Co-planar surface electrode designs,^{25–27} where sensing electrodes are deposited on the same side of the substrate, constrain the sensitive region to one surface. Since the goal of this work is to detect sub-surface implants at depths $\ll 1 \mu\text{m}$, we based the design of our single ion detector on a co-planar geometry.

Our detectors consist of co-planar metal electrodes and alignment marks, for subsequent registration, deposited on electronic grade diamond substrates from Element Six.²¹ In order to minimize defects near the surface which contribute to CCE degradation and memory effects,²² we followed the process described in Ref. 28 for removing the surface layer of the sample and polishing the resulting surface by reactive ion etching (RIE). We use an Ar/Cl_2 plasma for material removal and an Ar/O_2 plasma for polishing. The process parameters for the Ar/Cl_2 plasma are 8 mTorr pressure, 400 W ICP power, 250 W RF power, and 25/40 sccm flow rates for the Ar and Cl_2 , respectively. The process parameters for the Ar/O_2 plasma are 10 mTorr pressure, 700 W ICP power, 100 W RF power, and 25/30 sccm flow rates for the Ar and O_2 , respectively. After surface preparation, atomic force microscope (AFM) measurements on the diamond sample give a surface roughness of $\sim 1 \text{ nm}$. The detector electrodes and alignment marks are patterned by standard optical lithographic techniques. The metal layer is deposited by electron beam evaporation of Ti/Pt/Au with thicknesses of 30/50/100 nm. Before measurements are made, the sample is cleaned with a piranha solution of $\text{H}_2\text{SO}_4:\text{H}_2\text{O}_2$ (3:1) for 5 min to remove any organics from the surface followed by a de-ionized water rinse. For this study, we varied both the gap between the electrodes ($2 \mu\text{m}$, $5 \mu\text{m}$, and $10 \mu\text{m}$) as well as the length of the electrodes ($50 \mu\text{m}$, $75 \mu\text{m}$, $100 \mu\text{m}$, and $125 \mu\text{m}$). In Figure 1(a), an optical image of a $10 \mu\text{m}$ gap detector used for this study is shown.

We modelled the process of a 200 keV Silicon implantation into diamond with SRIM. In Figure 1(b), the resulting range and ionization profiles of such a simulation is plotted. We modelled the electric fields generated in the device for a given bias using the Silvaco Atlas TCAD program.²⁹ From Eq. (1), the relevant component of the electric field for detection is the x component whose magnitude across the gap varies from 6 to $20 \text{ V}/\mu\text{m}$. In Figure 1(c), cut lines of the magnitude of the x component of the electric field at a depth of $\sim 100 \text{ nm}$ in the substrate are plotted for both 10 V and 100 V biases. The result of this simulation is comparable to the simulation in Ref. 25. Based on simulations represented

by Figure 1(c) and the value of the carrier saturation field, $1 \text{ V}/\mu\text{m}$, for bulk diamond,³⁰ a bias range of 10 to 100 V is sufficient to expect a CCE of $>95\%$ in for the devices while remaining well below the breakdown field strength of $1 \times 10^3 \text{ V}/\mu\text{m}$.³⁰

We characterize the detectors using 200 keV Silicon ions from the nanoImplanter (nI). The nI is a 100 kV focused ion beam system (A&D FIB100NI) with a liquid metal alloy ion source (LMAIS), ExB filter, Raith lithography stage, fast blanking/chopping system, and electrical probes. The ExB filter allows for the selection of the species and charge state of ions from the LMAIS for the beam with $\Delta M/M > 61$. For this work, the Si^{++} charge state is used with an accelerating potential of 100 kV resulting in a 200 keV Silicon beam on target. The Raith lithography stage allows for the precise positioning of the beam on the detector where the spatial resolution is limited by the beam spot size. For the experiments described in this paper, the beam spot size was measured to be $<40 \text{ nm}$ at full-width at half maximum. The fast blanking and chopping system allows for range of pulse lengths from $<16 \text{ ns}$. The procedure to set the average number of ions per pulse is to measure the dc beam current with a femto-ammeter (Keithley 6430) and adjust the beam pulse length to achieve the average number of ions per pulse desired using the fast blanking and chopping system. The nI is also equipped with electrostatic beam deflection plates for lateral scanning of the beam allowing for ion beam induced charge (IBIC)³¹ collection maps. Electrical connections to the detector are made with in-situ probes (Kleindiek MM3A). The current induced on the electrodes of the detector is converted to a voltage pulse using a charge sensitive pre-amplifier (Amptek A250CF). From SRIM¹⁷ calculations, a single 200 keV Silicon ion will generate $\sim 10\,000 \text{ e}^-/\text{h}$ pairs in diamond (using $13.3 \text{ eV}/\text{e}^-/\text{h}$ pair³²). This will result in a $\sim 7 \text{ mV}/\text{ion}$ signal at the output of the pre-amplifier. Scaling the output by the number of implanted ions per pulse and any subsequent amplification allows for the calculation of the CCE. All measurements were performed at nominally normal incidence in the [100] plane of the diamond substrate.

The detectors are characterized by taking IBIC line scans through the gap, as indicated in Figure 1(a), as a function of bias. For these experiments, an average of 100 ions per pulse was used to measure the CCE. This was done to strike a balance between an uncertainty in the number of ions per pulse and the introduction of significant substrate lattice damage. From Poisson statistics, we can expect a

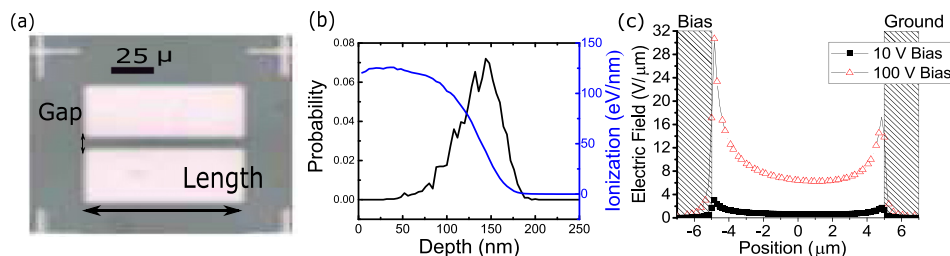


FIG. 1. (a) Image of one of the devices tested with a gap of $10 \mu\text{m}$ and a length of $100 \mu\text{m}$. The vertical arrow in the figure indicates the direction of the line scans taken in Figures 2(a)–2(c). (b) SRIM simulation of a 200 keV Si ion in diamond. The black line is the probability distribution of the implanted ions and the blue line is the ionization profile. (c) Cut lines showing the x component of the TCAD electric field simulation at 100 nm depth for two bias conditions.

$\sim 10\%$ uncertainty in the IBIC signal for on average 100 ions per pulse since the signal height will be proportional to the number of ions per pulse. We estimate the CCE loss from damage to be 0.5% per ion by performing repeated line scans and measuring the signal reduction over the same area. As a result, the maximum CCE expected is 50% for these experiments.

Figures 2(a)–2(c) show representative line scans at a scaled bias (the bias divided by the gap size) of $10\text{ V}/\mu\text{m}$ for the three different gaps. The CCE is largest near the edges of the electrodes and drops off near the center. To explain the shape of the CCE as a function of impact point, we performed a simple IBIC simulation displayed in Figure 2(d). The electric field and Gunn potential were calculated using COMSOL³³ and then a line of charge was created according to the SRIM ionization profile. The carriers were followed and the induced charge was calculated as a function of time using the Gunn potential difference³⁴ and carrier lifetime. Using a surface layer of 100 nm, corresponding to the ionization profile, with a reduced carrier lifetime (10–100 ps) resulted in a similar profile as experimentally measured. For comparison, typical carrier lifetimes in CVD diamond are on the order of 10 ns in the bulk.²³ From the simulation, the CCE is enhanced near the edges due to a non-negligible vertical component of the electric field driving carriers below the surface layer. At this point, we did not attempt to match the experimental results but show qualitatively that this mechanism leads to a similar profile.

Figure 3(a) shows a plot of CCE versus scaled bias for the three different gap sizes ($2\ \mu\text{m}$, $5\ \mu\text{m}$, and $10\ \mu\text{m}$).³⁵ The CCE saturation curve as a function of bias is used to establish the optimum bias for detector operation.²⁰ The CCE saturates, reaching the expected 50%, at $5\text{ V}/\mu\text{m}$ in Figure 3(a), and this is in the range of observed fields for velocity saturation in high grade CVD diamond^{21–23} for all the gaps when plotted versus scaled bias. The continued CCE increase above saturation is most likely due to the Frenkel-Poole effect since we are applying a field well above the threshold for detrapping observed in previous studies³⁶ while the

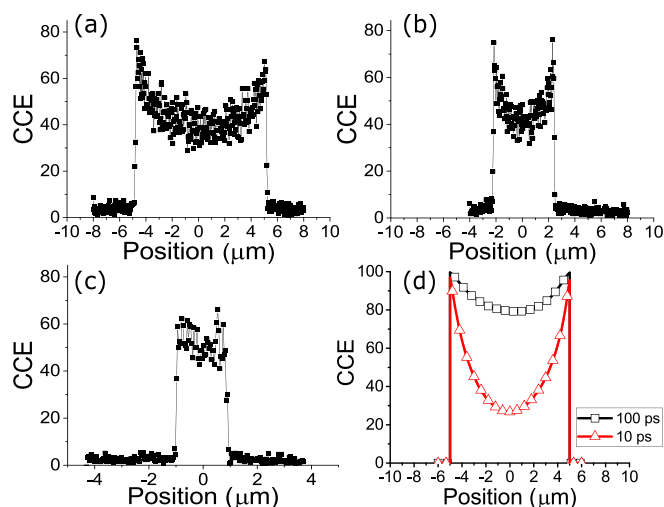


FIG. 2. IBIC line scans taken across devices with (a) $10\ \mu\text{m}$, (b) $5\ \mu\text{m}$, and (c) $2\ \mu\text{m}$ gaps using 100 ions per pulse with a scaled bias of $10\text{ V}/\mu\text{m}$ (the bias divided by the gap size). (d) CCE simulation with reduced carrier lifetimes (10 and 100 ps) in the shallow implantation region.

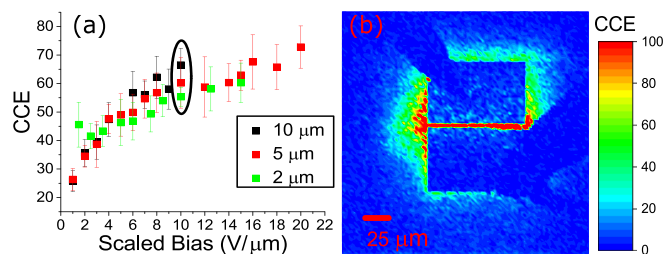


FIG. 3. (a) Plot of the peak CCE per pulse versus scaled bias as a function of gap size. The black oval indicates the data displayed in Figs. 2(a)–2(c). (b) IBIC image of a $2\ \mu\text{m}$ gap detector, taken with $15\text{ V}/\mu\text{m}$ and on average 10 ions per pulse. The CCE in the gap region approaches 100%. The probe tips connecting to the detector as well as the electrodes are visible in the image.

applied electric field is an order of magnitude below the threshold to generate appreciable impact ionization.³⁷ Detrapping rather than carrier generation is the most likely explanation for the increasing CCE above saturation.

Figure 3(b) shows an IBIC map of a $2\ \mu\text{m}$ gap detector taken at a $15\text{ V}/\mu\text{m}$ bias and with an average of 10 ions per pulse irradiation. In the figure, the outline of the detector electrodes and probe tips used to contact to the detector are clearly visible due to the detection in the periphery of the device. Within the gap of the detector, the CCE approaches 100%.

To resolve single ions, we first lower the average beam current to less than on average one ion per pulse and collect the detector response for approximately 1000 pulses where the beam position is stepped by 100 nm after each pulse to minimize the effects of substrate damage. A histogram of such an experiment is displayed in Figure 4(a). The peaks of the histogram are fitted with Gaussian curves. The signal-to-noise ratio (SNR) for the one ion peak is ~ 3.2 , where the SNR is defined as

$$SNR = \frac{\mu_{\text{signal}}}{\mu_{\text{noise}} + \sigma_{\text{noise}}}. \quad (2)$$

μ_{signal} is the average signal value, μ_{noise} is the average noise value, and σ_{noise} is the half-width at half maximum of the noise peak. The Poisson probabilities for 0, 1, 2, 3, and 4 ions for an on average 0.65 ions per pulse match the experimental counts to within 3%. To optimize the detection system for single ion counting, the average beam current per pulse is further reduced to an average of 0.2 ions per pulse. In this regime, most pulses contain no ions and the pulses with ions either have one or two ions per pulse. We added a high gain spectroscopy amplifier (Ortec 671) to the detector chain to minimize the overlap of the single ion response with the noise peak increasing the effective gain by a factor of 600. Figure 4(b) displays a histogram of the results with Gaussian fits to the signal peaks. The normalized signal peaks match the Poisson probabilities for 0.2 ions per pulse to within 3%. The optimized detection scheme results in an SNR of 7.3 for the one ion signal with an energy resolution of 20 keV.

Figure 4(c) displays an oscilloscope trace of a signal pulse from a single ion event which can be used to count in ions to the substrate following the procedure described in Ref. 14. This technique would result in a counted implantation with an

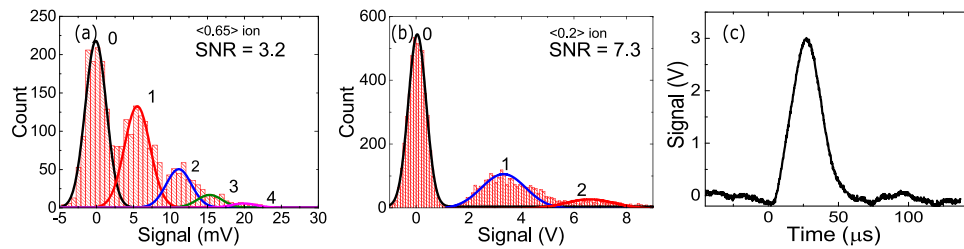


FIG. 4. (a) Histogram of the detector response for less than one ion per pulse with a $2\ \mu\text{m}$ gap device. The solid curves are Gaussian fits to the peaks. The amplitudes of the peaks match the Poisson distribution for an average of 0.65 ions per pulse. (b) Histogram of the detector response after the gain of the detector electronics is increased to maximize the sensitivity for single ions and the pulse duration of the beam is reduced to minimize the probability of more than one ion per pulse. The solid lines are Gaussian fits to the peaks where the amplitudes correspond to the Poisson distribution for an average of 0.2 ions per pulse. (c) An oscilloscope trace of the detector response to a single ion showing visibly of 45 (ratio of the peak height to the background).

expected error rate of $\sim 1\%$ based primarily on the overlap between the 1 and 2 ion peaks as the overlap between the 0 and 1 ions peaks leads to negligible 0.0005% error. This error rate can be further reduced through lowering the average number of ions per pulse to $\ll 0.01$ giving a probability of 2 or more ions per pulse to be $< 0.005\%$ allowing for reliable single ion detection.

In conclusion, we have fabricated and characterized a series of co-planar diamond detectors optimized for sub-200 keV Si detection. We demonstrated quantized single ion detection with a SNR approaching 10 for implantation conditions that will allow for coupling between a counted number of ions and diamond nano-photonic structures. Based on the achieved SNR, we anticipate that this technique would also be applicable for counting Nitrogen ions with a comparable fidelity. SRIM simulations indicate that there would be a sufficient number of electron hole pairs generated to detect a Nitrogen implantation at a depth suitable for coupling to a photonic cavity. From this, we can estimate the lower bounds of detectability with an expected SNR of 2 and resolve a 60 keV Si implantation at a depth of $42 \pm 12\ \text{nm}$ or a 50 keV N implantation at a depth of $63 \pm 15\ \text{nm}$. For lower energy detection, SNR improvements can be achieved through the use of in-vacuum detector electronics, cooling the detector, and, potentially, by channeling the implantation along the crystallographic axis.²⁰ The single ion detection capability demonstrated here will allow for counted ion implantation which reduces the uncertainty in the color center yield by removing the Poisson distribution of the number of implanted ions. This should allow for a systematic understanding of how to improve the yield of single color centers by co-implantation, varying annealing parameters and surface termination to be developed.^{10,11,15,16}

We would like to thank B. Doyle for helpful discussions on data analysis and B. Pate of the Naval Research Laboratory for advice on diamond surface preparation. Additionally, we would like to thank J. Nogan, W. Ross, and A. James of the Center for Integrated Nanotechnologies for assistance with fabrication. This work was performed, in part, at the Center for Integrated Nanotechnologies, a U.S. DOE Office of Basic Energy Sciences user facility. Sandia National Laboratories is a multi-program laboratory operated by Sandia Corporation, a Lockheed-Martin Company, for the U.S. Department of Energy under Contract No. DE-AC04-94AL85000.

¹F. Jelezko and J. Wrachtrup, "Single defect centers in diamond," in *Physics and Applications of CVD Diamond* (Wiley-VCH, 2008).

²R. Schirhagl, K. Chang, M. Loretz, and C. L. Degen, *Annu. Rev. Phys. Chem.* **65**, 83 (2014).

³F. Shi, Q. Zhang, P. Wang, H. Sun, J. Wang, X. Rong, M. Chen, C. Ju, F. Reinhard, H. Chen, J. Wrachtrup, J. Wang, and J. Du, *Science* **347**, 1135 (2015).

⁴A. M. Zaitsev, *Phys. Rev. B* **61**, 12909 (2000).

⁵A. Sipahigil, K. D. Jahnke, L. J. Rogers, T. Teraji, J. Isoya, A. S. Zibrov, F. Jelezko, and M. D. Lukin, *Phys. Rev. Lett.* **113**, 113602 (2014).

⁶R. E. Evans, A. Sipahigil, D. D. Sukachev, A. S. Zibrov, and M. D. Lukin, *Phys. Rev. Appl.* **5**, 044010 (2016).

⁷S. Pezzagna, D. Rogalla, D. Wildanger, J. Meijer, and A. Zaitsev, *New J. Phys.* **13**, 035024 (2011).

⁸S. Sangtawesin, T. O. Brundage, Z. J. Atkins, and J. R. Petta, *Appl. Phys. Lett.* **105**, 063107 (2014).

⁹S. Tamura, G. Koike, A. Komatsubara, T. Teraji, S. Onoda, L. McGuinness, L. Rogers, B. Naydenov, E. Wu, L. Yan, F. Jelezko, T. Ohshima, J. Isoya, T. Shinada, and T. Tani, *Appl. Phys. Express* **7**, 115201 (2014).

¹⁰S. Pezzagna, B. Naydenov, F. Jelezko, J. Wrachtrup, and J. Meijer, *New J. Phys.* **12**, 065017 (2010).

¹¹D. Antonov, T. Häußermann, A. Aird, J. Roth, H. R. Trebin, C. Müller, L. McGuinness, F. Jelezko, T. Yamamoto, J. Isoya, S. Pezzagna, J. Meijer, and J. Wrachtrup, *Appl. Phys. Lett.* **104**, 012105 (2014).

¹²D. N. Jamieson, C. Yang, T. Hopf, S. M. Hearme, C. I. Pakes, S. Praver, M. Mitic, E. Gauja, S. E. Andresen, F. E. Hudson, A. S. Dzurak, and R. G. Clark, *Appl. Phys. Lett.* **86**, 202101 (2005).

¹³J. A. Seamans, E. Bielejec, M. S. Carroll, and K. D. Childs, *Appl. Phys. Lett.* **93**, 043124 (2008).

¹⁴E. Bielejec, J. A. Seamans, and M. S. Carroll, *Nanotechnology* **21**, 085201 (2010).

¹⁵B. Naydenov, V. Richter, J. Beck, M. Steiner, P. Neumann, G. Balasubramanian, J. Achard, F. Jelezko, J. Wrachtrup, and R. Kalish, *Appl. Phys. Lett.* **96**, 163108 (2010).

¹⁶J. Schwartz, S. Aloni, D. F. Ogletree, and T. Schenkel, *New J. Phys.* **14**, 043024 (2012).

¹⁷J. F. Ziegler, J. P. Biersack, and M. D. Ziegler, *The Stopping and Range of Ions in Matter* (Ion Implantation Press, 2008).

¹⁸R. G. Wilson, *Surf. Coat. Technol.* **47**, 559 (1991).

¹⁹J. B. Gunn, *Solid-State Electron.* **7**, 739 (1964).

²⁰G. F. Knoll, *Radiation Detection and Measurement* (Wiley, 2000).

²¹See www.ef.com for "Element Six".

²²A. Lohstroh, P. J. Sellin, S. G. Wang, A. W. Davies, J. Parkin, R. W. Martin, and P. R. Edwards, *Appl. Phys. Lett.* **90**, 102111 (2007).

²³H. Pernegger, "High mobility diamonds and particle detectors," in *Physics and Applications of CVD Diamond* (Wiley-VCH, 2008), pp. 309–325.

²⁴M. Marinelli, E. Milani, A. Paoletti, A. Tucciarone, and G. Verona Rinati, *Appl. Phys. Lett.* **75**, 3216 (1999).

²⁵P. J. Sellin and M. B. Breese, *IEEE Trans. Nucl. Sci.* **48**, 2307 (2001).

²⁶S. G. Wang, Q. Zhang, Q. Wang, S. F. Yoon, J. Ahn, Q. Zhou, D. J. Yang, and J. Q. Li, *Diamond Relat. Mater.* **12**, 682 (2003).

²⁷J. Forneris, A. Lo Giudice, P. Olivero, F. Picollo, A. Re, M. Marinelli, F. Pompili, C. Verona, G. Verona Rinati, M. Bennetti, D. Cannata, and F. Di Pietrantonio, *Europhys. Lett.* **108**, 18001 (2014).

²⁸Y. Chu, N. P. de Leon, B. J. Shields, B. Hausmann, R. Evans, E. Togan, M. J. Burek, M. Markham, A. Stacey, A. S. Zibrov, A. Yacoby, D. J. Twitchen, M. Loncar, H. Park, P. Maletinsky, and M. D. Lukin, *Nano Lett.* **14**, 1982 (2014).

- ²⁹See <http://www.silvaco.com> for “Silvaco TCAD”.
- ³⁰C. J. Wort and R. S. Balmer, *Mater. Today* **11**, 22 (2008).
- ³¹M. B. Breese, E. Vittone, G. Vizkelethy, and P. J. Sellin, *Nucl. Instrum. Methods, Sect. B* **264**, 345 (2007).
- ³²P. Olivero, J. Forneris, M. Jaksic, Z. Pastuovic, F. Picollo, N. Skukan, and E. Vittone, *Nucl. Instrum. Methods, Sect. B* **269**, 2340 (2011).
- ³³See <http://www.comsol.com> for “COMSOL: Multiphysics Modeling and Simulation”.
- ³⁴E. Vittone, Z. Pastuovic, P. Olivero, C. Manfredotti, M. Jaksic, A. Lo Giudice, F. Fizzotti, and E. Colombo, *Nucl. Instrum. Methods, Sect. B* **266**, 1312 (2008).
- ³⁵Experiments were also performed with changing the length of the detector. There was no noticeable change in the detector response with changing the length.
- ³⁶M. Girolami, A. Bellucci, P. Calvani, R. Flammini, and D. M. Trucchi, *Appl. Phys. Lett.* **103**, 083502 (2013).
- ³⁷A. Hiraiwa and H. Kawarada, *J. Appl. Phys.* **114**, 034506 (2013).